Airborne interferometer for atmospheric emission and solar absorption

David W. Keith, John A. Dykema, Haijun Hu, Larry Lapson, and James G. Anderson

The interferometer for emission and solar absorption (INTESA) is an infrared spectrometer designed to study radiative transfer in the troposphere and lower stratosphere from a NASA ER-2 aircraft. The Fourier-transform spectrometer (FTS) operates from 0.7 to 50 μm with a resolution of 0.7 cm^{-1}. The FTS observes atmospheric thermal emission from multiple angles above and below the aircraft. A heliostat permits measurement of solar absorption spectra. INTESA's calibration system includes three blackbodies to permit in-flight assessment of radiometric error. Results suggest that the in-flight radiometric accuracy is ~0.5 K in the mid-infrared. © 2001 Optical Society of America

OCIS codes: 280.0280, 010.3920, 000.2170, 120.3180, 120.5630.

1. Introduction

We have designed and tested an interferometer for emission and solar absorption (INTESA) intended to test models of atmospheric radiative transfer, to detect trace constituents in the troposphere and lower stratosphere, and to serve as a temperature and humidity sounding system. The Fourier-transform spectrometer (FTS) can cover a spectral range from 0.7 to 50 μm (14,000 to 200 cm^{-1}) with a resolution of 0.7 cm^{-1}. With overlapping detectors, the instrument has continuous spectral coverage in the 3–50-μm region. It measures atmospheric emission from above and below the aircraft; in addition, it measures the atmospheric absorption in the direct solar beam.

INTESA fills an unusual niche in the evolution of airborne infrared spectrometers. The design of previous airborne infrared spectrometers has focused either on meteorological sounding or on the detection of trace atmospheric constituents. Instruments for meteorological sounding typically have a spectral resolution between 0.3 and 3 cm^{-1}; observe only the most important bands for sounding, from ~4 to 15 μm [e.g., the High-Resolution Interferometer Sounder[1] (HIS) and the National Polar-Orbiting Operational Environmental Satellite System Airborne Sounder Testbed-Interferometer[2] (NAST-I)]; and observe only below the aircraft. Instruments for detection of trace constituents typically have spectral resolutions at least an order of magnitude higher (e.g., of the order of 0.01 cm^{-1}) and typically operate either in emission [Fourier-Transform Infrared Sounder (FIRS[3])] or solar absorption (Mark-IV[4]) but not both. INTESA has a resolution comparable to modern sounding instruments (e.g., NAST-I), but has poorer sensitivity and is not designed for cross-track scanning. Unlike a typical sounding instrument, INTESA can observe emission at various angles above and below the aircraft and can also observe the solar beam, allowing both tracer observations and atmospheric sounding.

The combination of (1) a spectrometer that can observe radiance above and below the aircraft and also measure column absorption in the solar beam with (2) a platform that can operate from the midtroposphere to the lower stratosphere provides a unique and powerful tool to test models of radiative transfer that are the basis of nadir sounding algorithms. The usual method of testing such systems is to compare nadir radiance measured from an aircraft with that computed based on temperature and humidity profiles measured by a sonde.[5] Although this method may be optimal for end-to-end testing of a retrieval system, it is less than optimal for testing the underlying radiative transfer models. INTESA permits an experimental design in which radiance and column absorption are measured on parallel flight tracks at two (or sever-

When this research was performed, all the authors were with the Department of Earth and Planetary Sciences, Harvard University, Cambridge, Massachusetts 02138. D. W. Keith (keith@cmu.edu) is now with the Department of Engineering and Public Policy, Carnegie Mellon University, Pittsburgh, Pennsylvania 15213-2670.

Received 16 November 2000; revised manuscript received 11 June 2001.

0003-6935/01/305463-11$15.00/0

al) altitudes. The resulting data overconstrains the radiation field, allowing analysis to be substantially less sensitive to uncertainties in the atmospheric profile that are often the dominant error in the nadir-only experiment.

The spectral region between 20 and 50 μm has been underexplored by existing airborne or spaceborne instruments, yet it is the key spectral region for radiative cooling of the upper troposphere. Uncertainty in radiative transfer in this region has significant implications for climate.[6] Experiments with INTESA will examine the spectroscopy of the water-vapor rotation band with the combination of emission and absorption observations described above.

The radiometric calibration system includes three blackbodies, one of which is designed to operate at cryogenic temperatures to provide an accurate zero reference. In the laboratory, INTESA has demonstrated internal radiometric consistency of significantly better than 0.5 K in the 300–1500-cm^{-1} spectral range. In flight, the accuracy in the mid-infrared is estimated to be approximately 0.5 K based on internal radiometric consistency and on agreement with the NAST-I instrument.[7]

Low weight, power consumption, and volume were among the key design goals because INTESA is designed to fly either on a NASA ER-2 high-altitude aircraft or on a remotely piloted aircraft. As flown on the ER-2 in 1998, the total weight of INTESA, including the instrument rack, was 60 kg.

2. Instrument Design

A schematic view of the instrument, including optics, detectors, and moving mirrors, is shown in Fig. 1. Five detectors share the interferometer's two output ports. The spectral range and scientific purpose of each detector are summarized in Table 1. In Subsections 2.A–2.H we first describe the optical design, detectors, and calibration; we then describe the electromechanical systems, first covering the heliostat, then the mechanical design, and finally the electronics and software.

A. Optical Design

1. Fore Optics

The optical system includes a pointing mirror as its first optical element. This mirror allows the spectrometer to view radiation from (1) the atmosphere above or below the aircraft, (2) the blackbodies, or (3) the solar beam reflected by the heliostat.

From scene to detector, ignoring folding mirrors, we arranged the optical system as shown in Fig. 2. The fore optics incorporate a three-element image relay. The first mirror forms an image of the scene on the field stop. In addition, it images the blackbody aperture onto the second mirror that acts as a field lens and is coincident with the aperture stop. The third mirror relays the image of the aperture stop (and the blackbody aperture) through the beam splitter into the plane of the corner-cube vertex. When we relay the image of the blackbody aperture to the plane of the corner-cube vertex, the system has a magnification of 1.2.

The three-optic image relay system requires one more optic than the more conventional two-optic telescope. It offers the following advantages: (1) A single aperture stop controls the beam waists at the blackbody aperture and corner-cube vertex. (2) The size of the beam waist at the blackbody is as small as is possible, consistent with the etendue of the interferometer and the desired field of view (FOV). Because this system does not place the field stop at the detector, it sacrifices some sensitivity but facilitates the achievement of high radiometric accuracy.

All the reflective optics except the heliostat mirrors are diamond-machined aluminum with a vacuum-deposited gold-on-chrome coating (Lumonics Optics, Ottawa, Canada). The mirrors are bonded to custom-designed aluminum mirror mounts. Because the heliostat mirrors are exposed to the free air stream and must be handled on every flight, they have a more robust coating. They are made by means of electroplating nickel on the aluminum substrate, diamond machining the surface, and then electroplating ~0.5 μm of gold (Hardric Laboratories, Waltham, Mass.).

The field stop for the infrared channels is located on a rotating wheel offering six choices of a field stop aperture or a specialized filter. The FOV can be changed in flight to effect the desired trade-off between the signal-to-noise ratio (SNR) and the resolution for a given detector. The filters are required for observation of the solar beam. For the mid-infrared, the standard external FOV is 57-mrad full angle—48-mrad FOV at the interferometer after demagnification in the image relay.

2. Interferometer

The interferometer is a custom Bomem midband (Bomem, Quebec, Canada), a permanently aligned right-angle Michelson interferometer. It features corner cubes mounted at right angles to each other on a wishbone structure that rotates around the beam splitter so that the cubes move in opposite directions along orthogonal optical axes. Its optical properties are summarized in Table 2. The custom-designed beam splitter is CsI with a flatness of λ/5 at 0.6 μm and a parallelism of ~2 μrad (Spectral Systems, Hopewell Junction, N.Y.). The high-index coating material is Si rather than Ge to allow transmission at 0.75 μm. The coating allows good fringe contrast at 0.75 μm at the expense of diminished performance at longer wavelengths where the reflectivity falls to 10% at 50 μm. The corner-cube faces are permanently aligned to an accuracy of 5 μrad and are flat to λ/10. The only required alignment, the relative position of the two corner-cube vertices, is performed by Bomem at the factory. First-order thermal expansion effects are removed because each arm of the wishbone is of equal length.

The wishbone is an aluminum structure that ro-

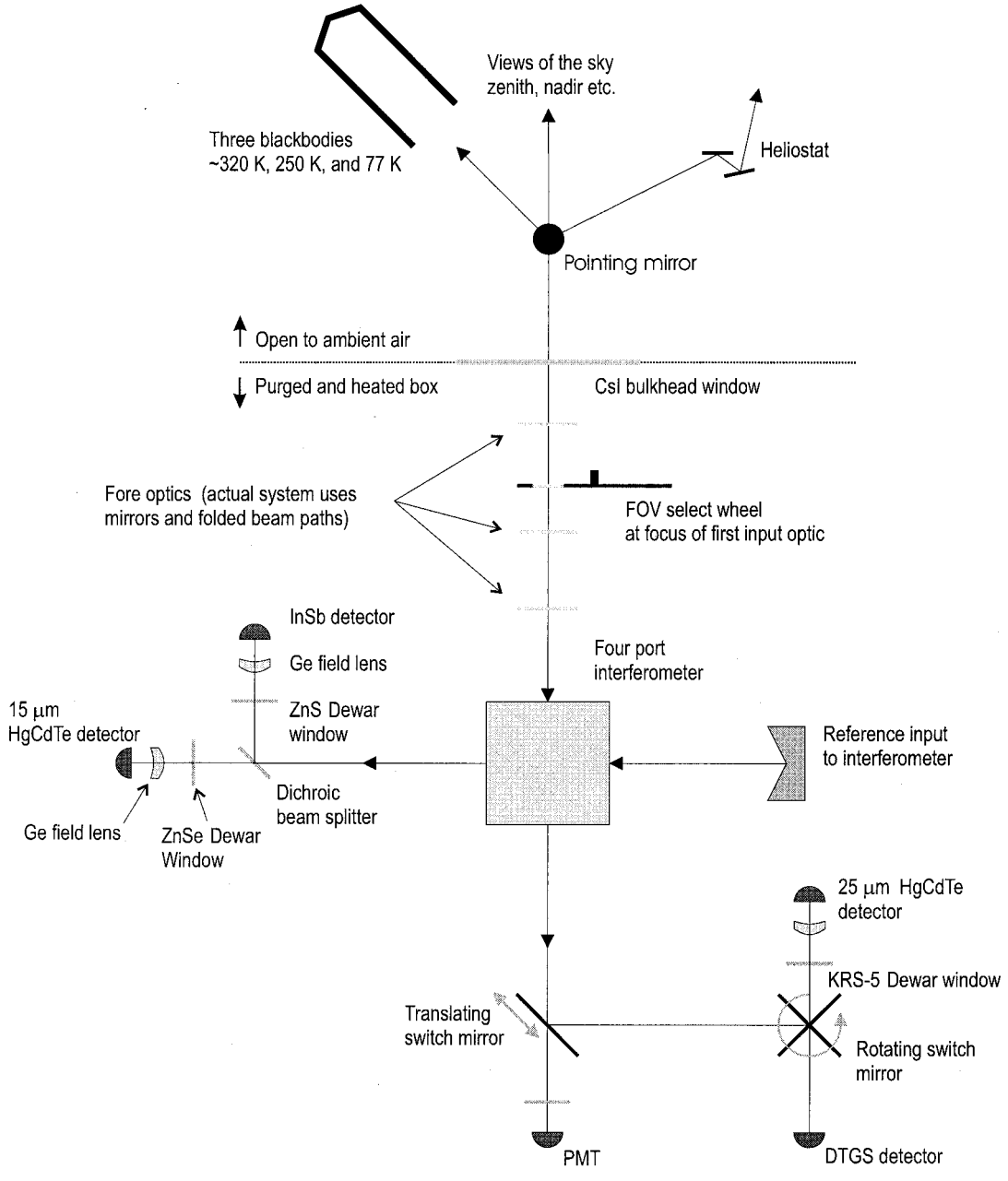

Fig. 1. Schematic of the full optical system. All transmissive optics and moving mirrors are indicated. Numerous flat folding mirrors are omitted, as are the focusing mirrors for the infrared detectors (shown as optic 4 in Fig. 2). A more detailed layout of the fore optics and interferometer is found in Fig. 2. The schematic substantially distorts the system geometry; for example, the three cryogenically cooled detectors (InSb, 15-μm HgCdTe, and 25-μm HgCdTe) are located in the same detector Dewar.

tates on a set of steel flexures driven by a solenoidal electromagnet on one of the arms. It has good inherent vibration insensitivity and high mechanical reliability. The system is balanced so that the center of mass is located at the flexure, effectively minimizing the susceptibility to linear vibrations. The interferometer core is mounted kinematically on three bolts, allowing the core to be easily removed and replaced; because the bolts must penetrate the optical plate, they are fabricated from titanium to minimize thermal distortions.

The interferometer is used in the Connes, or four-port, configuration in which the two complementary inputs and outputs are physically separated. One input comes from the pointing mirror through the fore optics. The other input comes from a blackbody source with good temporal stability but no radiometric accuracy. The two outputs feed separate detector systems (Fig. 1).

A 0.5-mW linearly polarized He–Ne laser in a hermetic vessel provides the optical reference for the interferometer. The He–Ne is packaged with its power supply in a cylindrical case, allowing a low-weight and low-volume pressure vessel.

Table 1. Summary of Detectors

Detector Name	Spectral Window (cm^{-1})	Spectroscopic Interest
PMT	13 120 ± 500	Oxygen *A* band for sounding cloud properties in reflected solar light.
InSb	1800–3500	Detection of HDO and other trace constituents in absorption. Emission and absorption from 4.3-μm CO_2 band.
MB HgCdTe 15 μm cutoff	700–1800	Window, 6.7-μm H_2O, O_3, and blue edge of 15-μm CO_2. Primarily in emission mode.
LW HgCdTe 25-μm cutoff	400–700	15-μm CO_2 and blue edge of H_2O rotation band. Emission only.
DTGS	200–400	H_2O rotation band.

Table 2. Summary of FTS Optical Properties

Optical Property	Value
Beam diameter at corner-cube vertex (cm)	2.5
Maximum half-angle at corner-cube vertex (mrad)	25
Etendue (cm^2 sr)	0.04
Beam-splitter material	CsI
Rate of change of OPD[a] (cm sec^{-1})	1 or 5
Fringe rate for 632-nm laser (kHz)	16 or 80
Maximum OPD[a] (cm)	±1.0
Unapodized resolution (cm^{-1})	0.60

[a]OPD, optical path difference.

B. Detectors

The spectrometer employs five detectors to cover the spectral range from 0.7 to 50 μm (Table 1). The detectors share the two output ports of the interferometer as shown in Fig. 1. The MB HgCdTe and the InSb share one interferometer output by use of a dichroic beam splitter. The long-wave- (LW-) HgCdTe, deuterated triglycine sulfate (DTGS), and photomultiplier tube (PMT) detectors share the other optical port by means of two movable mirrors. Detector characteristics are summarized in Table 3.

The two HgCdTe detectors and the InSb are mounted in a single Dewar with three optical ports. The liquid-nitrogen Dewar offered significant advantages over mechanical cryocoolers, including freedom from vibration and electrical pickup, reliability, and provision of dry-nitrogen boil-off.

A pyroelectric detector is used to cover the band from 25 μm, the LW cutoff of the HgCdTe detectors, to 50 μm, the LW cutoff of CsI. Pyroelectric detectors do not need cooling, are highly reliable, are linear, and offer nearly black spectral responsivity. However, they have low detectivity and are sensitive to acoustic noise.

To mitigate the influence of aircraft vibrations, the pyroelectric detector is mounted along with its objective mirror on a vibration-isolating mount with a resonant frequency of ~35 Hz. Despite the isolator, aircraft vibration significantly degrades the detector performance.

The high linearity of the pyroelectric detector is key to the laboratory demonstration of high radiometric accuracy described in Section 3.A. It serves as a linear standard that allows more robust diagnosis and correction of radiometric error that is due to nonlinearity in the photoconductive HgCdTe detectors.

The five detectors employ three different kinds of optical system. Three cryogenically cooled detectors (two HgCdTe's and an InSb) each use a system like

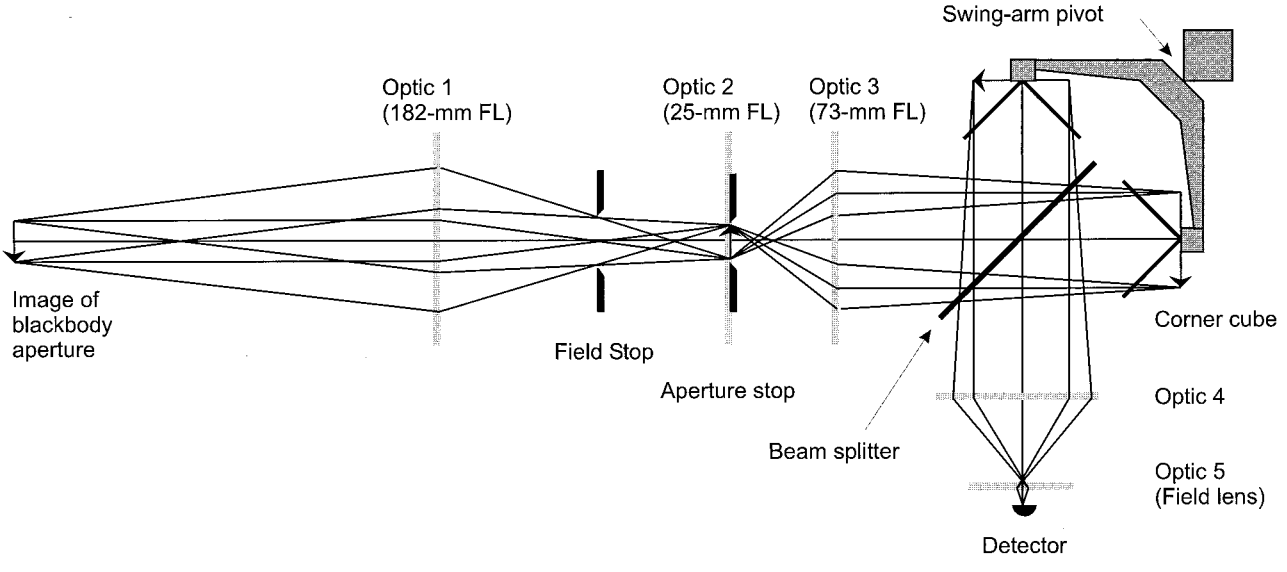

Fig. 2. Schematic of the optical system for a single cryogenic detector. All folding mirrors, except those in the interferometer core, are omitted. Optics 1–4 are illustrated as thin lenses but all are, in fact, mirrors with spherical or parabolic surfaces. The schematic shows the layout of the Bomem midband interferometer projected onto a single plane. In fact, the beam exiting the interferometer is translated into the page one beam diameter so that optic 4 and the detector are on a different plane from optics 1–3. FL, focal length.

Table 3. Detector Specifications

Detector	Detectivity (D*)[a]	Cutoff (μm)	Dimensions	Type	Vendor
PMT	1-nA dark current 20–40% quantum efficiency	1.0	5-mm diameter	PMT	Hamamatsu, Bridgewater, N.J.
InSb	1.4×10^{11} D*	5.5	1.5-mm diameter	PV[b]	EG&G Judson, Montgomery, Pa.
MB HgCdTe	4.4×10^{10} D*	15	1-mm^2	PC[c]	Belov Technology, New Brunswick, N.J.
LW HgCdTe	4.7×10^{9} D*	26.5	2-mm^2	PC[c]	EG&G Judson, Montgomery, Pa.
DTGS	3.0×10^{8} D*	NA[d]	2-mm diameter	Pyroelectric	GEC-Marconi, Southampton, UK

[a]D* is in units of cm $Hz^{1/2}$ W^{-1}, and noise-equivalent power is in units of W $Hz^{-1/2}$. All values are at a frequency of 1 kHz.
[b]PV, photovoltaic.
[c]PC, photoconductive.
[d]NA, not available.

that depicted in Fig. 2, in which the final optic is an *f*-number ~0.7 field lens. It is nonimaging to ensure that the sky is not imaged onto the detector. This prevents inhomogeneity in the detector sensitivity from causing inhomogeneity in the system responsivity across the FOV. This is important to achieve a symmetric instrument line-shape function. We optimized the shape and placement of the field lens using three-dimensional ray tracing to meet the dual constraints of minimizing the beam spot on the detector while ensuring that rays from each point in the sky are distributed evenly across the detector surface.

The solar band PMT detector employs a glass lens to couple the interferometer output into a 0.5-mm-diameter optical fiber with a FOV of 10 mrad. This signal is delivered to the PMT through a second lens to fill the detector's active area. The field stop for the PMT is provided by the active area of the optical fiber.

The DTGS pyroelectric detector is located at the focus of a 44-mm-diameter parabolic mirror with a 38-mm focal length. The FOV of the detector and mirror system is large enough that light reaching the detector from the scene is controlled by the field stop in the fore optics.

C. Radiometric Calibration System

The radiometric design is constrained by the dual goals of (1) high radiometric accuracy on bright sources, primarily nadir views, and (2) low zero offset needed to look at thin clouds above the aircraft. To realize these goals the instrument carries three blackbodies. Two warm blackbodies, maintained at ~240 and ~310 K, bracket the range of observed nadir brightness temperature allowing optimal calibration for the nonlinear photoconductive detectors. Accurate determination of radiometric zero demands a cryogenic blackbody because the equivalent temperature of a typical thin cirrus cloud at 900 cm^{-1} is ~120 K. Most importantly, use of three blackbodies allows in-flight estimation of end-to-end radiometric error.[8]

The warm blackbodies are each built around an aluminum tube with a 120° opening-angle concave cone at its end. The blackbodies have an entrance aperture of 2.5 cm, an interior diameter of 3.5 cm, and a length of 7.5 cm, giving a length-to-aperture aspect ratio of ~3. The interior surfaces are treated by Enhanced Martin Black (Lockheed Martin, Denver, Colo.) that has a total reflectance of less than 3% between 3 and 50 μm. The estimated on-axis emissivity is >0.998. To achieve temperature uniformity, the blackbody is suspended only by its entrance end with a low-conductivity mount. The blackbodies are heated with thermofoil heaters and are insulated with ~1.5 cm of Nomex and polyimide foam. Thermostatic control is accomplished with software. Temperatures are measured at four points along the blackbody. Temperature uniformity in flight is ~0.5 K between the midpoint of the blackbody cylinder and the endcap when the blackbody is ~100 K warmer than ambient.

The cryogenic blackbody core is 10 cm long, but is otherwise similar to the blackbody cores described above. Its estimated[9] on-axis emissivity is >0.999. The blackbody Dewar permits direct optical access to the blackbody core that is mounted in a toroidal liquid-nitrogen vessel. The Dewar is 15 cm in diameter by 15 cm long with a dry mass of 2.7 kg and a hold time of ~30 hr. Both blackbody and detector Dewars were supplied by Kadel Engineering, Danville, Ind. Ice buildup and the creation of ice or liquid fog are prevented by a shutter mounted on the face of the Dewar in combination with a continuous purge of dry nitrogen provided by boil-off from the Dewar. In operation, a dry-nitrogen purge is established prior to Dewar filling, and the shutter is opened only when required for calibration.

Blackbody temperatures are measured with high-stability thermistors (superstable, 4600 series, YSI, Yellow Springs, Ohio). When operated at <340 K these thermistors have a temperature drift of <0.01 K in eight years. Primary temperature calibration to National Institute of Standards and Technology-traceable standards was performed by YSI. Accuracy was checked by a comparison of YSI thermistors with different resistances, β coefficients, and encapsulation technologies and by comparison with thermistors supplied by other vendors. Comparisons with several thermistors on an isothermal mount demonstrated that the end-to-end

system accuracy—including readout electronics—was better than 0.05 K. The readout electronics compare the thermistors with reference resistors that have an accuracy of 250 parts per million and a temperature coefficient of 10-parts per million K^{-1}. The effects of reference voltage drift, or drift in analog-to-digital converter gain, are thus eliminated to first order.

D. Heliostat

The heliostat directs the solar beam into the instrument by the pointing mirror. The optical design allows the tracking of the overhead solar beam to solar zenith angles of 50°–70°, depending on the aircraft heading. The design differs from that of heliostats for balloonborne instruments that are typically designed to look near the horizon.[10] The tracking is achieved by two independent mirrors, a design that affords overall compactness and is also lightweight. Each mirror is driven by a stepper motor with a microstepper drive that has a resolution of 0.1 mrad. The heliostat optomechanical assembly weighs a total of 1.7 kg, with an additional 1.1 kg for the associated electronics.

The heliostat is positioned in an opening in the skin of the ER-2 superpod, which necessitates its removal when the instrument is loaded or unloaded. A kinematic mounting system ensures angular repeatability of <1 mrad for each installation of the heliostat assembly. The opening in the superpod skin exposes the heliostat to the airstream during flight, requiring thermal control for the motor and bearing assemblies. This is achieved with thermofoil heaters.

A pickoff mirror directs a small portion of the solar beam through a lens that images it onto the face of a position-sensitive detector from Hamamatsu Photonics of Bridgewater, N.J. This sensor allows a servo loop to keep the solar beam aligned along the optical axis.

Servo control is achieved by a digital control loop implemented at 10 Hz. The control loops for the two axes operate independently. The control algorithm includes procedures to locate the solar beam by a raster scan over the entire solid angle visible to the heliostat and to actively servo the mirrors to lock the solar beam parallel to the optical axis. The position-sensitive detector detects the solar beam when it is within 100 mrad of the optical axis, allowing the heliostat to typically locate and lock onto the Sun in <1 min.

During typical flights, the heliostat locked on the solar beam for 50–90% of the flight time, depending on the details of the flight path. The typical rms pointing noise was 4 mrad compared to the solar image size of 9 mrad and instrument FOV of ~50 mrad. (Note that this pointing noise is acceptable because the narrow FOV PMT detectors do not observe the solar beam.)

E. Environmental Control and Gas Handling

Use of hygroscopic optics (CsI), needed to extend the spectral range to 50 μm, requires that the interior of the instrument maintain good thermal stability and low relative humidity. Thermal control is effected by use of multiple thermofoil heaters (Minco Products, Inc., Minneapolis, Minn.), arrayed in three zones surrounding the warm instrument enclosure. Each zone has a maximum power of ~100 W. Temperatures in the warm enclosure are monitored with 15 thermistors. The thermostatic control is in the software (with a hardware backup) to allow simple adjustment of the zones to achieve maximum thermal uniformity.

Boil-off of nitrogen from the Dewars provides ~1 STP l/min of dry gas to purge the optics. A single regulator maintains the Dewars at 1-bar pressure. The regulator is an active system comprising an absolute pressure transducer, control electronics, and a solenoid valve packaged with redundant burst disks to protect against overpressure. Flow from the regulator is split between the warm enclosure (where it is directed onto the interferometer beam splitter), the cold side of the bulkhead window, and the cryogenic blackbody.

In an unpressurized system, substantial purge flow is required to keep the optics dry during rapid descent from the cold upper troposphere. Use of Dewar boil-off for purging was a key design decision. Dewars hold much more gas per unit flown weight than do high-pressure bottles. An alternative design would have used mechanical cryocoolers for the detectors and a hermetically sealed instrument enclosure that required no purge gas (e.g., NAST-I[2]). For INTESA, the combination of Dewars and an unpressurized instrument housing saved substantial weight as we describe in Subsection 2.F.

F. Mechanical Design

INTESA is designed to fly in the rear of a NASA ER-2 superpod or in the nose payload bay of an Aurora Perseus remotely piloted aircraft (Aurora Flight Sciences Corp., Manassas, Va.). The INTESA system comprises four units: the instrument (36 kg), heliostat (3 kg), flight computer (7 kg), and the aircraft interface box (3 kg). The computer and aircraft interface are described in Subsection 2.G. Achieving low-flown weight is critical to both for unmanned aerial vehicle applications and for participation in large, weight-limited ER-2 deployments. As flown on the ER-2 in 1998, the total instrument weight including the instrument rack and all electrical cabling was 60 kg.

All components of the instrument are mounted on a single structural plate oriented normal to the direction of flight (Fig. 3). The 71 cm by 58 cm plate is fabricated with graphite-reinforced epoxy face sheets on a 2.5-cm-thick aluminum honeycomb core (Zivko Aeronautics, Guthrie, Okla.). The forward-facing side of the plate contains the fore optics, interferometer, all detectors, and various interface electronics all contained in an environmentally controlled enclosure. The enclosure is 1.2 cm thick, fabricated with graphite face sheets on a foam core. The aft side of

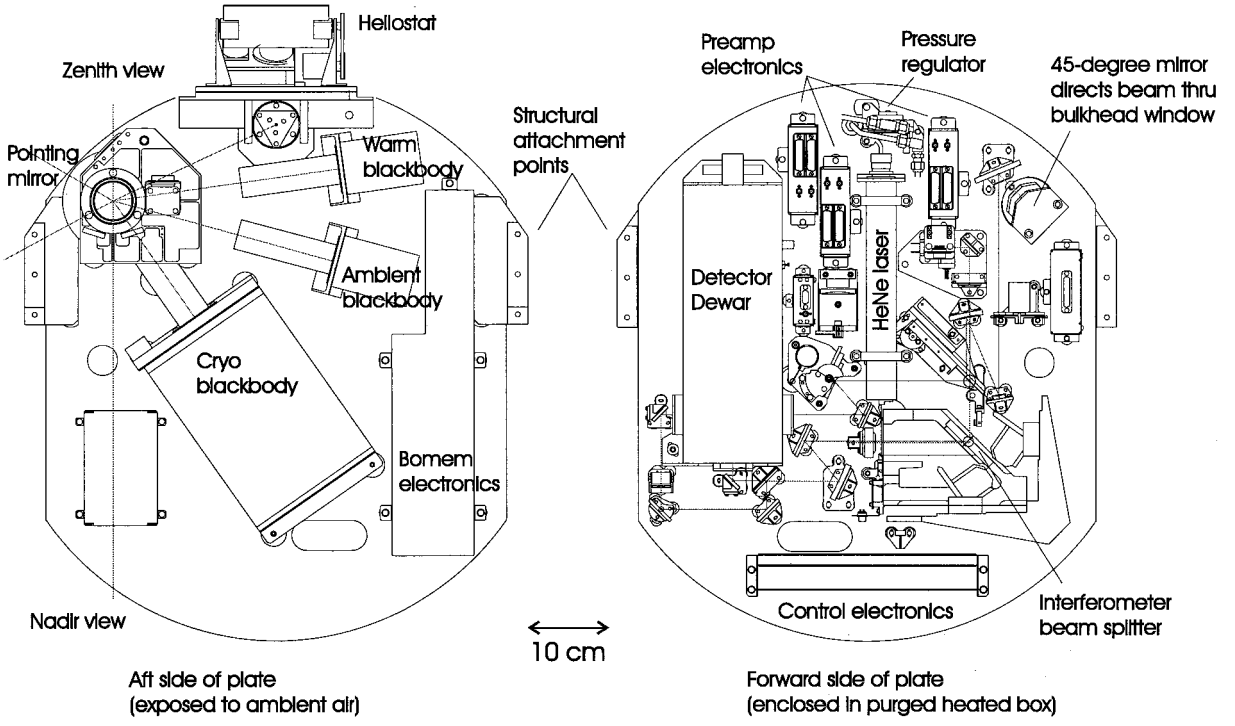

Fig. 3. Mechanical layout of INTESA showing components on both sides of the optical plate. The illustration is derived from computer-aided design drawings, so the geometry is exact—note the 10-cm-scale key.

the plate holds the pointing mirror, blackbodies, and heliostat.

Stepper motors are used for the pointing mirror, heliostat mirrors, and FOV wheel. The motors are operated with microstepping drivers (Intelligent Motion Systems, Inc., Marlborough, Conn.). Position reference is provided by optical switches in each assembly. At instrument start, and periodically thereafter, the motors are driven until a switch transition is detected to provide a position reference. Typical angular accuracy is ± 2 mrad. The shutter on the cryogenic blackbody and the two switch mirrors in the optical system use brushless dc motors with an integrated gearbox and controller (API Portescap, Switzerland).

The instrument is mounted to the ER-2 instrument rack with shock damping mounts with a resonant frequency of ~50 Hz. Two retractable doors are mounted on the ER-2 fairing to protect the heliostat and zenith view ports from the elements during ground operations and low-altitude flight.

G. Electronics

The flight computer is a 100-MHz i486 single-board computer that supports a stack of five custom PC-104 format interface cards. The computer uses a 1.2-Gbyte, 2.5-in. (6.4-cm) format hard drive in a pressure vessel. Together the interface cards provide 80 analog inputs (12-bit resolution), 20 analog outputs, 100 digital inputs and outputs, and interface electronics for 12 stepper motors. The high-rate interferogram data are delivered from the Bomem sampling electronics over a RS422 link to a Bomem-supplied industry standard architecture bus card in the flight computer.

The flight computer, a main signal distribution panel, and the dc-to-dc power supplies are contained in a single enclosure with a volume of ~30 l and a mass of 6.5 kg. Control of aircraft power and the cockpit interface are handled in a separate smaller box. All other instrument interface electronics, including the Bomem-supplied boards, are located in warm enclosures on the instrument structural plate.

Closed-loop control of the interferometer scan arm is accomplished by a Bomem-supplied board that also includes the 16-bit analog-to-digital converter for the sampling of the interferograms. The preamplifiers are a modified Bomem design with digital gain control. A custom multiplexer board after the preamplifiers permits two detector channels to be sampled at once, each at one sample every two laser fringes (normally 40 kHz). This board permits selection of any two of the six detector channels under software control.

The instrument operates on 28-V aircraft power. In the ER-2 configuration, a cockpit switch operates a relay in the INTESA aircraft interface box that supplies switched power to the instrument. Independent of the state of the relay, the instrument draws keep alive power for thermostatic heaters as long as aircraft wing power is present. The mean power requirement is 600 W.

H. Flight Software

The flight software runs under the QNX real-time, multitasking operating system (QNX Software Sys-

tems, Kanata, Ont., Canada). Custom compilers and support software built around a data-flow architecture allow high-level instrument control algorithms to be modular and to execute closed-loop control of many separate subsystems running at different rates. For example, the flight algorithm sequences observations of various detectors and pointing mirror targets (blackbodies, sky, heliostat) while simultaneously maintaining closed-loop thermal control of five subsystems at 0.25 Hz and closed-loop control of the heliostat at 10 Hz.

On the ER-2, the instrument operates completely autonomously with no telemetry. The only communication is with the pilot through a single fail light that is illuminated when the software detects a hardware failure or when low-level hardware detects that the software is nonresponsive. The software supports telemetry and remote-command capability, a facility we expect to use in future missions.

The software schedules observation sequences based on flight data, primarily aircraft altitude, as determined by an onboard pressure transducer. For example, less observing time is devoted to zenith observations when the aircraft is at high altitude, and observations are focused on the column absorption measurements with the heliostat when the aircraft is climbing or descending. Control of observation sequencing is readily changed according to the science objectives of a given flight.

3. Performance

To date INTESA has made 13 flights on three ER-2 deployments. Electrical, environmental, and computer systems have all performed well. The most serious problem has been the performance of the DTGS pyroelectric detector. Despite the vibration isolation system, the SNR has not been satisfactory to accomplish the science goals. We are retrofitting the detector system permit use of a liquid-He-cooled Dewar that will be fitted with Zn- and Cu-doped germanium photoconductive detectors that have been specially fabricated at Lawrence Berkeley National Laboratory. In Subsections 3.A and 3.B we present some representative data and discuss the radiometric calibration.

A. Radiometric Calibration

Systematic errors in the radiometric calibration of INTESA were investigated in the laboratory and in flight. Laboratory measurements test the inherent limitations of the radiometric calibration system aiding the diagnosis of radiometric errors found in flight. The laboratory tests with the highly linear DTGS detector allow accurate characterization of nonlinearity in the MB-HgCdTe detector. The resulting correction for nonlinearity in the photoconductive detectors is less ambiguous than is the case when correction depends on the photoconductive detectors alone.

In laboratory tests we used the instrument's three-

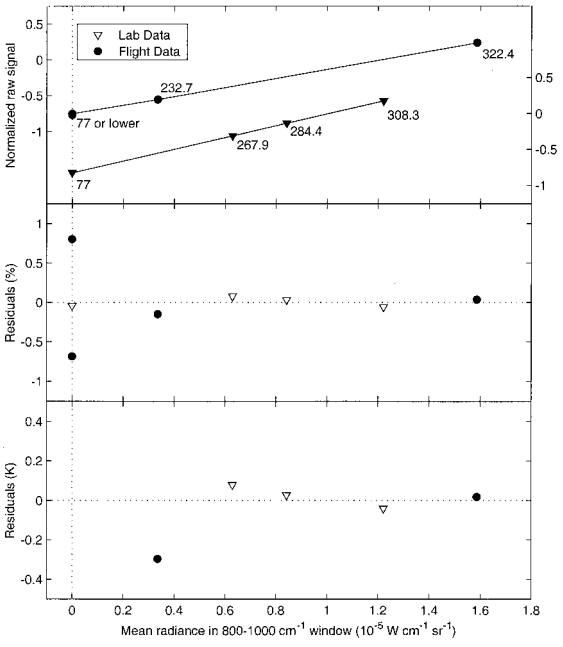

Fig. 4. Assessment of radiometric consistency. All three panels show the same flight and laboratory data, averaged over the 800–1000-cm^{-1} spectral window. The x axis shows the mean radiance in this spectral window of the Planck function evaluated at the measured blackbody temperature, except for the cryogenic blackbody and the zenith view for which zero radiance is assumed. (At cruise altitude the zenith view is effectively a deep-space view in the window region.) The top panel plots the raw signal. The points are labeled with the corresponding blackbody or scene temperature. The left-hand y axis corresponds to the upper curve (flight data); the right-hand y axis corresponds to the lower curve (laboratory data). The signals are phase corrected by use of the complex phase angle of the warmest blackbody to correct all others; the value plotted is the real part of the results with the minimum-to-maximum range of the signal normalized to unity. The middle panel shows the residuals from a linear fit to the data, equivalent to the residual radiance error at each point normalized to the full-scaled radiance. The lower panel shows the residuals in equivalent temperature units. The zero radiance points are omitted because their equivalent temperature error is infinite.

blackbody calibration system supplemented with an external laboratory blackbody designed to exceed the performance of the internal blackbodies. The estimated[9] emissivity of the laboratory blackbody is >0.9995. Temperature homogeneity within the core is better than 0.05 K, and thermometric error was <0.03 K. To avoid atmospheric absorption, experiments were performed in a dry-nitrogen atmosphere.

When more than three blackbodies are used, we can readily assess the errors by plotting the raw signal in a given spectral band versus the blackbody radiance in that band as predicted by the Planck function at its measured temperature, with a data point for each blackbody. Figure 4 shows flight and laboratory data in this format. Laboratory results from the DTGS detector typically show radiometric consistency between the four blackbodies of ~ 0.15 K across the spectral region from 300 to 1500 cm^{-1},

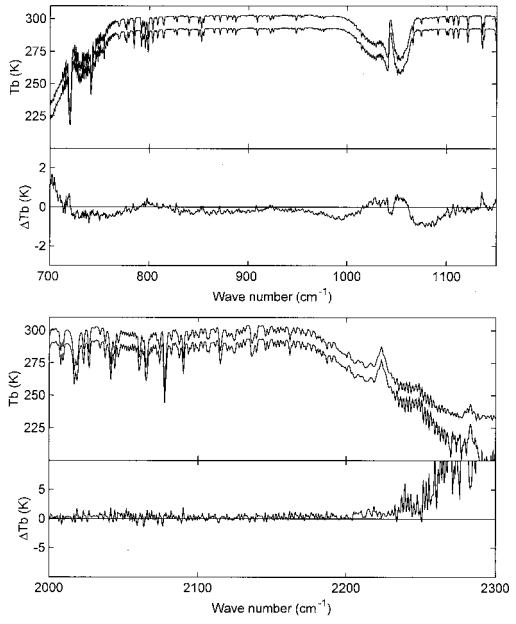

Fig. 5. Comparison of radiance measurements from INTESA and NAST-I. The spectra are nadir views over the clear-sky ocean. They were acquired from an ER-2 flight out of Wallops Flight Facility, 23 August 1999, at an altitude of 50 hPa, at 40 °N 73 °W. The plots show two different frequency ranges. In the upper panel of each plot the INTESA data are shifted upwards by 10 K, which puts them above the NAST-I data. The differences (INTESA − NAST-I) are shown on the lower panel of each plot. This figure is abstracted from a more detailed account of the INTESA–NAST-I intercomparison.[7]

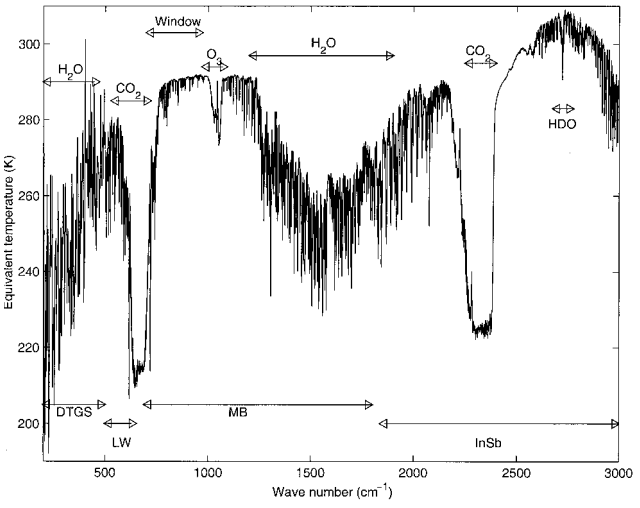

Fig. 6. Cloud-free nadir spectra from cruise altitude over the Pacific Ocean. The data are from 17 °N 121 °W at a 21-km altitude, except the DTGS data that are an average for the entire flight. The key at the bottom indicates which of four detectors is plotted, where LW and MB are the 25- and 15-μm cutoff HgCdTe detectors.

equivalent to a relative consistency in radiance of 1 in $\sim 10^3$ in the mid-infrared.

Radiometric consistency in flight can be assessed similarly with the three internal calibration sources and the zenith view, where the zenith radiance in the stratosphere in the atmospheric window regions is assumed to be zero. Typical results are shown in Fig. 4.

Radiometric accuracy is more difficult to assess. A general heuristic to assess the accuracy is to measure the same quantity with multiple instruments that use different physical measurement methods so that their systematic errors can be assumed to be uncorrelated. When it is assumed that random error has been eliminated, the critically analyzed disagreement between measurements serves as a diagnostic test of accuracy. Use of multiple blackbodies and the agreement between flight and laboratory blackbodies—which use different means of construction and independent thermometry—suggest that the demonstrated radiometric consistency is a fair measure of true radiometric accuracy. In-flight comparison with the NAST-I instrument shows radiometric consistency of better than 0.5 K based on nadir views in the atmospheric window regions (Fig. 5). However, the limited quantity of overlapping NAST-I and INTESA measurements precludes us from drawing firm conclusions about the systematic differences between the instruments. The data nevertheless support the conclusion that the in-flight accuracy of both instruments may be better than 0.5 K under some conditions.[7]

In normal operation the instrument calibration and complex phase correction are derived from the observation of two blackbodies by use of a linear fit of the instrument offset and responsivity (complex numbers) as at each spectral point.[11] After nonlinearity correction, calibration, and phase correction, we estimate that the radiometric accuracy on weak spectral lines is ~0.5% in the 425–3000-cm^{-1} spectral range using the LW- and MB-HgCdTe and the InSb detectors.

B. Representative Data

Figure 6 shows calibrated nadir emission spectra. The broad, 4–50-μm spectral range of these emission spectra allows direct comparison of nadir sounding between the 4- and 15-μm bands of CO_2 and between the rotational and the 6.7-μm bands of H_2O. Figure 7 shows the sensitivity of the instrument in emission mode. Figure 8 shows solar spectra. The top panel shows data recorded with the heliostat; the data are on a log scale to demonstrate the SNR of ~500:1 in 1 s at 1-cm^{-1} resolution. The absorption data were used to detect trace constituents, such as HDO and CO in the upper troposphere, and to test the temperature dependence of absorption in the 4.3-μm CO_2 band edge that is of critical importance for atmospheric sounding.[12] The ability to take the ratio of absorption spectra measured at different altitudes to measure absorption in an atmospheric layer bracketed by two aircraft flight tracks is key to these analyses.

4. Summary

We have demonstrated an airborne interferometric spectrometer with a novel combination of features,

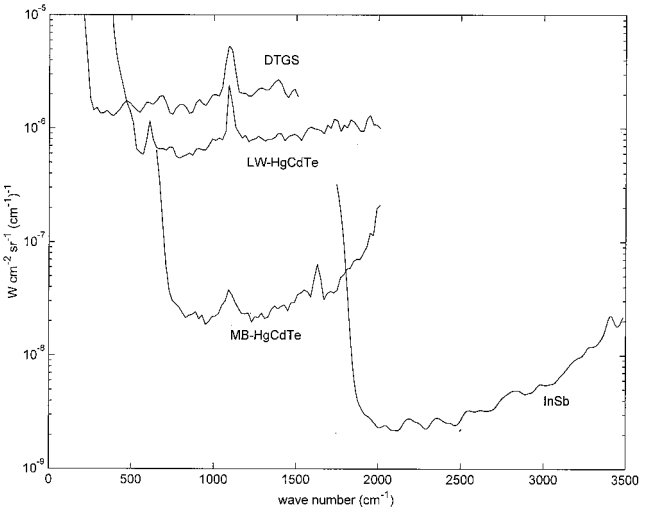

Fig. 7. Measured noise-equivalent spectral radiance (NESR) of the infrared detectors. NESR is in units of W cm^{-2} sr^{-1} (cm^{-1})$^{-1}$ at a spectral point spacing of 0.5 cm^{-1} (unapodized resolution of ~0.7 cm^{-1}) with 1-s total interferogram acquisition time. Data are from the laboratory, and flight results differ by no more than 30%, except for the DTGS. Typical flight spectra are recorded with 8-s integration giving 2.8 times lower NESR.

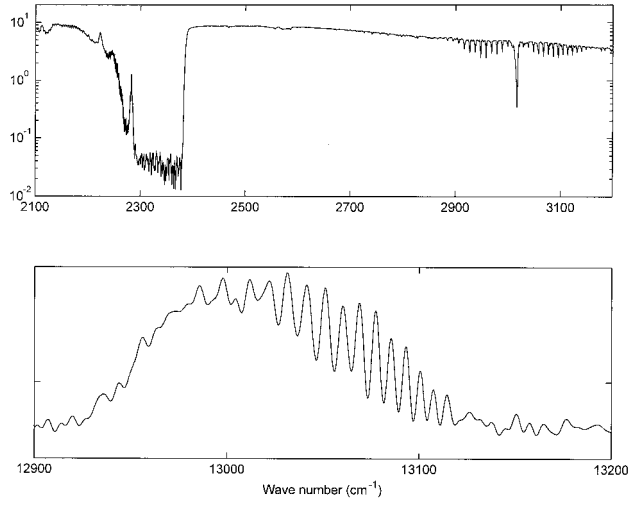

Fig. 8. Solar spectra in the upper panel shows solar absorption viewed through the heliostat with the InSb detector from an altitude of 9.9 km with a solar zenith angle of 56°. The signal is shown on a log scale to demonstrate the SNR. Note that the broad absorption maximum in the 2300–2400-cm^{-1} region is bounded at the high-frequency end by the 4.3-μm CO_2 band edge. CH_4 is visible between 2900 and 3100 cm^{-1}. The lower panel shows the *A* band of atmospheric O_2 at 0.76 μm observed at sea level with the PMT. The instrument observed the sky through a diffuse reflecting surface (white paper).

including the measurement of atmospheric emission at multiple angles above and below the aircraft; the measurement of absorption in the solar beam; the measurement of reflected solar spectra; and finally, use of multiple blackbodies to overdetermine the radiometric calibration. The instrument has been demonstrated in flight. Based on limited data, nadir radiance measurements from INTESA are in close agreement with simultaneous observations by NAST-I. We anticipate that INTESA will provide new data on the radiative properties of thin cirrus clouds and new tests of radiative transfer in the water-vapor rotation band. Analysis of infrared solar absorption spectra will provide a new tool to measure trace constituents from the ER-2 that will complement existing *in situ* measurements.

We depended on the strengths of the Harvard engineering team; we thank Norton Allen, Joe Demusz, Mike Greenberg, Jim Oliver, Marco Rivero, and Eileen Schomp. We thank Henry Buijs and Andre Villemaire at Bomem for their expert guidance. We thank the ER-2 pilots, Jim Barrilleaux, Ken Broda, Bill Collette, Jan Nystrom, and Dee Porter, as well as the ground crew for their unequaled professionalism. Finally we thank our scientific collaborators, Danny Kirk-Davidoff and Ryan Spackman and the NAST-I investigators, particularly Bill Smith and Bob Knuteson, for their willing collaboration. This research was supported under NASA grant NAG-1-1849.

References

1. H. E. Revercomb, D. D. LaPorte, W. L. Smith, H. Buijs, D. G. Murcray, F. J. Murcray, and L. A. Sromovsky, "High-altitude aircraft measurements of upwelling IR radiance: prelude to FTIR from geosynchronous satellite," Mikrochim. Acta **2,** 439–444 (1988).
2. D. Cousins and W. L. Smith, "National Polar-Orbiting Operational Environmental Satellite System (NPOESS) Airborne Sounder Testbed-Interferometer (NAST-I)," in *Application of Lidar to Current Atmospheric Topics*, A. J. Sedlacek and K. W. Fischer, eds., Proc SPIE **3127,** 323–331 (1997).
3. D. G. Johnson, K. W. Jucks, W. A. Traub, and K. V. Chance, "Smithsonian stratospheric far-infrared spectrometer and data reduction system," J. Geophys. Res. **100,** 3091–3106 (1995).
4. G. C. Toon, "The JPL MkIV interferometer," Opt. Photon. News **2,** 19–21 (1991).
5. L. L. Strow, D. C. Tobin, W. W. McMillan, S. E. Hannon, W. L. Smith, H. E. Revercomb, and R. O. Knuteson, "Impact of a new water vapor continuum and line shape model on observed high resolution infrared radiances," J. Quant. Spectrosc. Radiat. Transfer **59,** 303–317 (1998).
6. A. Sinha and J. E. Harries, "The Earth's clear-sky radiation budget and water vapor absorption in the far infrared," J. Clim. **10,** 1601–1614 (1997).
7. H. Hu, J. Dykema, D. Keith, L. Lapson, J. Anderson, R. O. Knuteson, and W. L. Smith, "Intercomparison of atmospheric radiance measurements by two Fourier transform spectrometers flown on the NASA ER-2," in *IRS2000: Current Problems in Atmospheric Radiation*, W. L. Smith and Y. M. Timofeyev, eds. (Deepak, Hampton, Va., 2001).
8. D. W. Keith and J. G. Anderson, "Accurate spectrally resolved infrared radiance observation from space: implications for the detection of decade-to-century-scale climatic change," J. Clim. **14,** 979–990 (2001).

9. R. J. Chandos and R. E. Chandos, "Radiometric properties of isothermal diffuse wall cavity sources," Appl. Opt. **13,** 2142–2151 (1974).
10. T. Hawat, C. Camry-Peyret, and R. Torguet, "Suntracker for atmospheric remote sensing," Opt. Eng. **37,** 1633–1642 (1998).
11. H. E. Revercomb, H. Buijs, H. B. Howell, D. D. LaPorte, W. L. Smith, and L. A. Sromovsky, "Radiometric calibration of IR Fourier-transform spectrometers: solution to a problem with the High-Resolution Interferometer Sounder," Appl. Opt. **27,** 3210–3218 (1988).
12. H. Hu, L. L. Strow, D. W. Keith, and J. G. Anderson, "Validation of radiative transfer for atmospheric temperature sensing," in *Tenth Conference on Atmospheric Radiation* (American Meteorological Society, Boston, Mass., 1999). Other representative data and analysis can be found at http://www.arp.harvard.edu/sci/rad.